Automation in Construction 141 (2022) 104467

Contents lists available at ScienceDirect

Automation in Construction

journal homepage: www.elsevier.com/locate/autcon

Compressive load-dominated concrete structures for customized 3D-printing fabrication

Alexander Lin [a], Abhimanyu Goel [a], De Hui Alwin Wong [a], Charlene Yeo [a], Jacky Chung [b], Sze Dai Pang [c], Chi-Hwa Wang [d], Hayden Taylor [e,f,*], Harn Wei Kua [a,*]

[a] Department of the Built Environment, National University of Singapore, 4 Architecture Drive, Singapore 117566, Singapore
[b] Industrial Centre, The Hong Kong Polytechnic University, Hung Hom, Kowloon, Hong Kong
[c] Department of Civil and Environmental Engineering, National University of Singapore, 1 Engineering Drive 2, Singapore 117576, Singapore
[d] Department of Chemical and Biomolecular Engineering, National University of Singapore; 4 Engineering Drive 4, Singapore 117585, Singapore
[e] Department of Mechanical Engineering, University of California, Berkeley, CA 94720. USA
[f] Berkeley Education Alliance for Research in Singapore, #11-01 CREATE Tower, 1 CREATE Way, Singapore 138602, Singapore

ARTICLE INFO

Keywords:
Concrete 3D printing
Arch
Unreinforced concrete
Thrust-line analysis
Modular construction

ABSTRACT

Existing approaches from design to concrete 3D-printing fabrication can customize the shapes of compression-dominated concrete arches and vaults but has limited applications due to high facility requirements such as a robotic arm and a reconfigurable print bed for fabricating overhanging geometries. Therefore, there is a need to develop an alternative design-to-fabrication approach for 3D printers without such facility requirements. In this paper, concrete blocks were designed as prismatic shapes which could be customized by a most basic, gantry-based 3D printer with a flat print bed and could be assembled to a larger 3D arch structure designed based on stability and strength analyses. The feasibility of such approach was demonstrated by lab prototyping. Reduced facility requirements in this approach allow 3D-printing to be more widely applied for customizing compression-dominated structures. With further design method innovation in the future, this design-to-fabrication approach can be extended for compression-dominated structures with more complex geometries.

1. Introduction

Concrete was one of the most widely used construction materials and it was well known to have much higher compressive than tensile strength (roughly by a factor of 10) [1]. Most types of contemporary concrete structures needed steel reinforcement to bear the tensile stresses experienced by the structures [2–4]. On the other hand, compressive load-dominated structure was a category of structure (such as arch and vault) with internal load transfer dominated by compression, leading to minimal internal tensile stress. Therefore, designing concrete structure as a compressive load-dominated structure allowed one to alleviate the requirement for incorporating steel reinforcement. In fact, medieval builders had been constructing unreinforced, compression-dominated arch and vault structures by assembling masonry blocks piece by piece [5,6]. Such structural form had attracted builders' and researchers' attention because it became a self-supported structure after assembling [5,7] and needed less or no steel reinforcement [5,7–10]. Reduction or elimination of steel reinforcement could lower the cost during construction and maintenance phase because steel reinforcement led to increased material and installation cost and was subjected to corrosion and fire-induced deterioration in concrete [9].

Arches and vault had traditionally been constructed from elemental blocks, such as bricks or tapered stones [11]. This approach was simple and allowed straightforward transportation of building materials to a construction site. However, customizing the curvature and dimension of these structures required manual adjustment during assembling of bricks and tapered stones [12]. Contemporary concrete arch and vault structures were commonly incorporated with modular design, where concrete modules were designed as custom shapes that could be assembled into the arch/vault shape [13]. Modular design led to faster and simpler construction process and improved member quality control [13]. By casting concrete modules directly into custom shapes, massive manual adjustment works for reaching the designed curvature of the

* Corresponding authors at: Department of Mechanical Engineering, University of California, Berkeley, CA 94720, USA; Department of the Built Environment, National University of Singapore, 4 Architecture Drive, 117566, Singapore.
E-mail addresses: hkt@berkeley.edu (H. Taylor), bdgkuahw@nus.edu.sg (H.W. Kua).

https://doi.org/10.1016/j.autcon.2022.104467
Received 21 May 2021; Received in revised form 19 June 2022; Accepted 26 June 2022
Available online 8 July 2022

structure were avoided. However, this required an additional step to build and set up customized formwork at the construction site or in a concrete precast factory. Except for a perfectly round arch and vault, the curvature of the concrete segments varied along the span of the structure [11,14], thus limiting the use of the same piece of mold for casting multiple segments.

To incorporate arches and vaults in different sites and buildings with different dimensions, there was a need for adjusting and customizing the dimensions of non-circular arch and vault structures [12,15,16]. Therefore, researchers sought to explore new approaches with integration of design tool and more variety of fabrication/construction technologies for building customized, compression-dominated structures. By using Grasshopper, a parametric design software, Borhani and Kalantar designed geofoam-based modules that could be fabricated by hot wire cutting and assembled into an arch [17]. A good modular design typically produced optimum sizes and dimensions of modules that could be stacked and efficiently occupy available space [18]; the study by Borgani and Kalantar achieved a modular design where the arch modules had customized shapes and they could be stacked into prismatic shapes that efficiently occupy the space on top of truck bed during transportation [17]. However, the components developed in this study were nonstructural geofoam arches; there was a need to explore an integrated design and fabrication scheme for customizing the components made by structural materials, such as concrete. Sousa and Martins developed an arch component which consisted of crok and glass-fiber reinforced concrete (GRC) modules respectively providing insulation properties and structural efficiency [19]. Since there was a need to cut expanded polystyrene foam into customized molds for making the complicated GRC modules, Grasshopper was used for 3D-modeling and designing the path of the hot-wire cutter. Mayencourt et al. made a more heavy-duty arch by casting UHPFRCC (Ultra-High Performance Fiber Reinforced Cement-based Composite) into a timber mold with a complicated shape [20]. Such mold consisted of timber panels interlocked together in non-orthogonal dihedral angles. An algorithm incorporated with Rhino3D was used to control the CNC milling process for fabricating these customized panels.

Thrust-line analysis was a tool that could be applied to design overall layouts of compression-only arch structures in 2D cases and validate their structural integrity. Such an analysis could find out the compressive force transfer pathway and thrust-line, thus ensuring compressive forces were transferred within the boundary in each arch segment [21–23]. To expand the application for designing contemporary 3D structures, such an analytical tool was applied to thrust network analysis (TNA) for 3D cases of compression-dominated structures [6]. Rippmann and Block utilized TNA to design freeform masonry-like vaults [24]. The feasibility of such approach was demonstrated by fabricating customized styrofoam blocks with 4-axes CNC wire cutter and assembling the blocks into a vault prototype. Bertetto and Riberi incorporated TNA into the design scheme for customized, lightweight vault structures with various amount and pattern of holes on top [25]. The mortar blocks in the small scale vault prototypes were casted in polylactide molds customized by fused filament fabrication. The usage of polymer-based molds generated plastic wastes and hence, induced relatively large environmental impact. Liew et al. integrated the processes of TNA and CNC-milling of customized molds for fabricating a compression-dominated, ribbed concrete floor system with arched supports [9]. CNC milling process for fabricating the customized formwork led to extra cost and time, thus rendering the fabrication process not ideal for making components with unrepeated geometries [10]. However, construction 3D-printing was especially suitable for fabricating this type of component [10,12,26,27]. Because 3D-printing was a formwork-free process for automatic material deposition [28,29], using such technology could avoid the high cost for fabricating customized formwork and eliminate the waste generated by formwork usage [30]. The geometry of 3D-printed building components was directly determined by the material deposition path controlled by the computer, and this could reduce the cost of generating complex shapes significantly [28,29]. This geometrical freedom not only opened more opportunities for creative shapes, but also enabled construction of structures in more efficient ways [27].

Rippmann et al. [10] sought to utilize particle-bed 3D printing of sand for prefabricating ribbed floor system, which was designed as five to seven modules assembled together through male-female interlocking features between them. Such a modular design was essential for prefabricated construction because the design divided a large component into smaller modules, which were not only lighter for easy transportation but also small enough for being fabricated monolithically in a 3D-printer with limited size [10]. This study demonstrated the capability of particle-bed 3D-printing technologies for achieving customized and modular design for compression-dominated structure. However, compared to particle-bed 3D printing [31], extrusion-based 3D-printing for cement/sand-based materials currently have not only higher technology readiness but also higher economic viability for rapid fabrication for building component [32]. Therefore, the extrusion-based technology is currently a more popular technology for construction 3D-printing [32,33] and was selected by many researchers as the technologies for fabricating shell and spatial concrete structures that were compression-dominated [8,12].

In the most prevalent form of extrusion-based 3D printing, concrete was extruded from a nozzle that was attached either to a 3 or 4-axis Cartesian robots [26] or to a 6 axis robotic arm [12,27]. The nozzle extruded concrete filaments along defined paths. When forming a building element, the paste-like filaments were stacked on top of a flat print bed layer-by-layer making it more challenging to print overhanging parts [12] existing in the vault and shell structures. Carneau et al. [12] developed a design framework to identify concrete filament extrusion path for complex structures and accordingly, 3D-printed concrete into partially self-supported, overhanging shapes forming dome and vault structures after the printings were completed. However, this approach required specific types of mortar with sufficiently good plastic viscosity to prevent plastic collapse of the freshly printed overhanging component, and a 6-axis robotic arm to move the mortar extrusion nozzle outside the horizontal plane [12]. In this study, the robotic arm continuously conducted 3D-printing to monolithically fabricate the sub-meter-scale structures. To deploy such an approach for 3D-printing of dome and vault structures with dimensions enlarged to about 5 m in size, the span of robotic arm needed to be scaled up accordingly. Instead of using 6-axis robot, Borg Constanzi et al. [8] sought to use a 4-axis Cartesian robots to 3D-print an unreinforced pavilion structure. In a typical 3D-printing process where concrete extrusion nozzle was moved by a 3 or 4-axis robot in horizontal plan for depositing each layer of concrete on top of a flat print bed, the 3D-printer stacked many consecutive concrete layers covered either same or progressively reduced areas, resulting a geometry without material overhanging. Lack of overhanging shape made such so-called “2.5D geometry” [12] (an example for forming such geometry is illustrated in Fig. 1) difficult to be directly deployed to build a shell structure. Therefore, Borg Constanzi et al. instead utilized a printing bed with reconfigurable curvature supporting the concrete filament printed along directions out of horizontal plane for 3D-printing of pavilion segments. However, usage of such reconfigurable printing bed increased the requirement for 3D-printing equipment. Besides, each segment for the pavilion structure was fabricated by 3D-printing the concrete segment contour but casting concrete in its core area; hence, the pavilion could only be considered as partially 3D-printed. To enable customized, compression-dominated structures to be more widely deployed in the construction industry, the next step is to incorporate its integrated design with a processing scheme that has higher scalability in the production line. Under this consideration, extrusion-based 3D-printing with higher productivity is preferred, compared to particle-bed 3D printing [32]. For design and 3D-printing of compression-dominated structures, the current solutions based on concrete extrusion technology need either

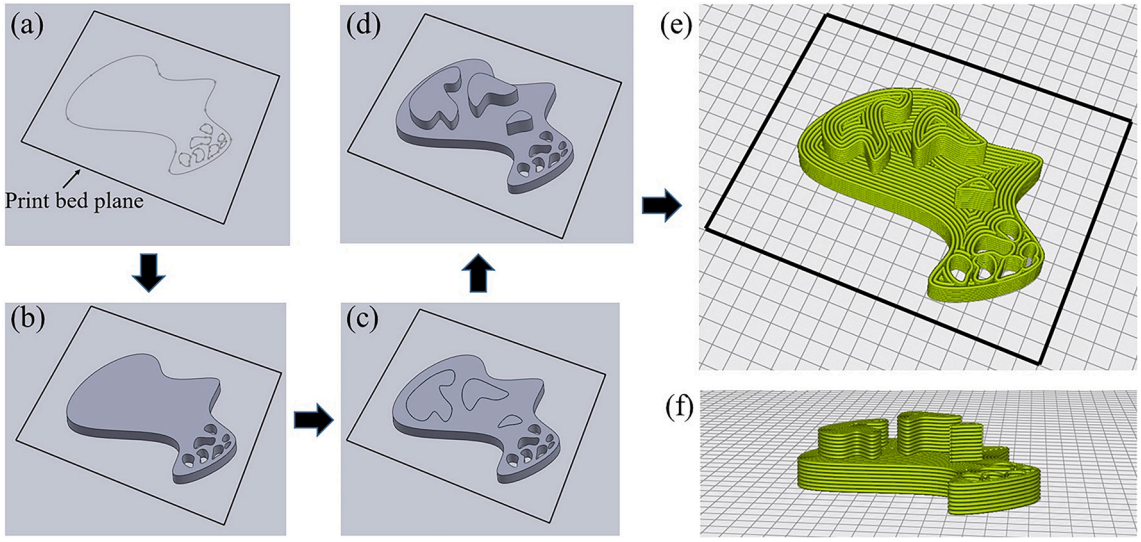

Fig. 1. 2.5D geometry can be developed according to step (a), (b), (c) and (d) and can be formed by stacking 3D-printed filament as shown by (e) and (f).

(1) specially designed concrete materials and a relatively costly robotic arm with 6-axis [12], or (2) a reconfigurable printing bed that may be complicated to be set up [8]. To remove these requirements that set a high threshold for mass customization of compression-dominated structures, there is a need to develop an integrated scheme for common flat-bed concrete extrusion printers with 3-axis gantry robot. This 3D-printing system is not only highly capable of rapidly customizing 2.5D components, but also has basic equipment requirements and hence reduces the cost of scaling up the future production line. This paper aims to utilize the design flexibility enabled by extrusion-based concrete 3D-printing for building up 3-dimensional, compression-dominated structures. The sizes of 3D-printing facility and its printing bed determine the maximum sizes of concrete components that can be printed. When a structure is larger than the printing facility, there is a need to print smaller components within the capacity of the 3D-printer and assemble the components into a larger structure. In this light, this paper focuses on a simple and systematic approach to design, fabricate and then assemble customized concrete elements into a large scale structure.

1.1. Scope of this paper

This paper is a proof of concept of a new approach for designing, fabricating and assembling of a compression-dominated 3D structure that consists of a pair of intersecting elliptical arches both with 2.5D geometries, whose shape designs were carried out based on an iteration process between shape adjustment and analyses for thrust-line and strength of the arch. Sub-meter-scale, 2.5D concrete segments with various curvatures/dimensions could be individually fabricated in a 3D-printer with limited print bed area (1×1 m of size), could be lifted/erected either by hand or small construction lift and then, could be interlocked to form the 3D structure that was about 5 m in size. To demonstrate the feasibility of manufacturing and assembling in the proposed approach, a physical prototype of such intersecting arches, which was scaled down to about 2.5 m in size, was fabricated by concrete 3D-printing; segments of this arch were partially assembled and then erected to form fully assembled structure. The feasibility was proved by the overall dimensions of the physical prototype being close to the design dimension in 3D-model. The overall approach enables customized, rapid and low-waste construction, and can provide a basis for creating more complex compression-dominated structures.

2. Development of arch structures

2.1. Design and analysis of 2.5D arch elements

The approach taken in this paper started with designing and analyzing arches under a 2D scenario as illustrated in Fig. 2 and such an arch was considered as a 2.5D geometry due to its consistent out-of-plane thickness. Shape design/adjustment of arch, thrust-line analysis and strength analysis were concurrently carried out in the design process of the proposed arch structure and are explained below:

(i) **Thrust-line analysis:** As shown by Fig. 2, the overall shape of an arch was determined by the direction of arch axis and the depth of arch. These two parameters were determined based on thrust-line analysis, which had been widely used in evaluating compression-dominated arch structures [6,21–23]. In such analysis, thrust-lines representing load paths of compressive force in the structure were calculated based on the load applied along the arch. If there was a group of thrust-lines that were always within the arch boundary (that is, between the boundaries set by extrados and soffit of the arch), the arch was compression-dominated [21–23]. If none of the thrust-lines were admissible to the arch, the arch was not compression-dominated and its design needed to be adjusted. The arch proposed in this paper was for sustaining its self-weight so the mass distribution along the arch would affect the direction of thrust-lines calculated based on load condition [23]. Therefore, adjusting the extrados and soffit not only affected the likelihood of finding admissible thrust-line between them but also affected the distribution of mass and self-weight along arch span, changing the profile of the thrust-line. Therefore, designing an arch by thrust-line analysis was an iterative process involving adjustments of many geometrical parameters following by the analyses.

(ii) **Decomposing structure into individual segments with customized geometries and internal voids:** Extrusion-based concrete 3D-printer in a prefab factory environment is commonly equipped with limited print bed area [34–36]. Such 3D-printer can only produce concrete component with a size up to a few meters and cannot monolithically fabricate an arch with a larger size. The large dimension and weight of such type of arch monolithically fabricated also increase the difficulty for delivery from prefabrication factory to the construction site. Therefore, the approach proposed in this paper decomposed the arch

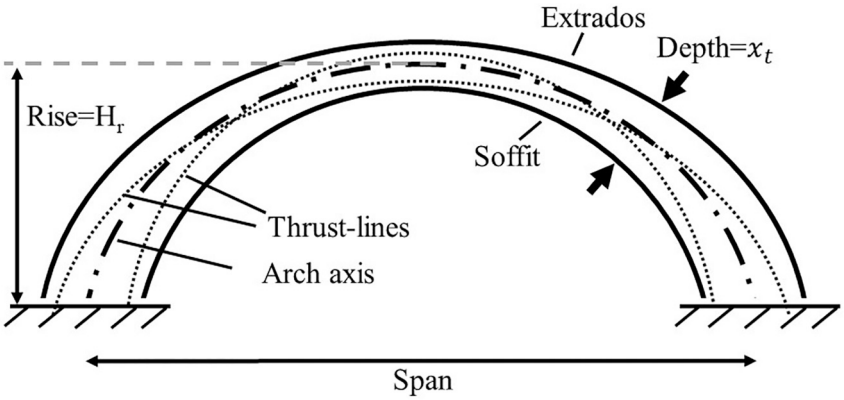

Fig. 2. Arch and thrust-lines.

geometries into individual, customized blocks, or 'segments' (as conceptually illustrated in Fig. 3a), which would, by limiting the largest segment dimensions such as s_1, s_2 and s_3 in Fig. 3a, fit comfortably within a 1 m square print bed. Within each segment, internal shape was also adjusted to include central voids (Fig. 3b) in the concrete elements to reduce mass.

(iii) **Strength analysis:** The arch structure was assembled by concrete segments and was not compression-dominated until it was fully assembled (Fig. 3a) so the loading condition for partially assembled arch (Fig. 3b) needed to be considered separately. Therefore, strength analysis was conducted for the arch – not only at the post-assembled stage, but also in the extreme case of the partially assembled stage to ensure that there were no structural failures.

In (ii) above, adjusting how the arch structure could be decomposed into different segments changed both total segment number and dimension/location of each segment. These also changed the arrangement and size of the void in each segment, thus affecting the self-weight distribution along the arch. This in turn led to a different load condition for strength analysis in (iii) and affected pathway of thrust-line for the analysis in (i). By carrying out an iterative process between geometry adjustments in (ii) and the analyses in (i) and (iii) (which considered the interactions between the geometry parameters and design constrains (such as maximum segment dimension limited by print bed area), the design for a slender, elliptical arch (Arch 1; Fig. 4) was developed. With such design procedure, this arch satisfied fabrication/construction feasibility and passed both strength and thrust-line analyses. This arch spanned about 5 m and had about 150 mm of out-of-plane block thicknesses; it had a 2.5D geometry and this design would be utilized to develop the 3D, double-arch structure in Section 2.2. To demonstrate the flexibility for the iteration process in adapting the design, this paper also reports a pointed arch (Arch 2; Fig. 5) geometries with 500 mm of out-of-plane block thicknesses developed via the design/analysis process.

Although both Arch 1 and Arch 2 were symmetrical, each segment on a given side of an arch had a unique set of dimensions (please refer to Fig. S1 in Supplementary Information in Appendix A), since the curvature of the arch design varied along the span (for example, radius of curvature changed from 2313 to 2570 mm from foundation to the top of Arch 1). The dimensional capabilities of today's concrete 3D printing processes were considered in the designs of the concrete segments. 26 mm of width and 12.5 mm of height were common dimensions of a concrete filament extruded by a typical concrete 3D printer. The 150 and 500 mm out-of-plane block thicknesses (for Arch 1 and 2 respectively) were designed based on the heights of concretes of 150 and 500 mm that could respectively be achieved by stacking 12 and 40 layers of concrete filaments. Such block thicknesses affected the weights of each concrete blocks. Therefore, they were used as input parameters representing the loading from self-weight for both thrust-line and strength analysis. When printing adjacent filaments parallel to each other, the print path for a filament could be designed to let small portion of its width overlap with the adjacent filament. Such a slight overlapping of filaments led to a stronger bonding at interface, with the side of adjacent filaments merging with each other and allowing some flexibility to adjust the total width of the filaments based on the amount of overlapping. For example, with 26 mm of width for individual filament, printing two parallel filaments with width overlapping of 4 mm (15.4% of single filament width) and 7 mm (26.9% of single filament width) respectively led to 50 and 45 mm of total widths for the two parallel filaments. Under this consideration, the minimum width (d_{min} in Figs. 4 and 5) of the features on the 3D-printed arch segments were set as the width of two filaments with less than 26.9% of individual filament widths overlapping with each other. These dimensions were large enough for being 3D-printed successfully; on the other hand, the overall sizes of individual segments were small enough to be produced with many existing flat-bed concrete extrusion printers. The segment designs were 2.5D geometry,

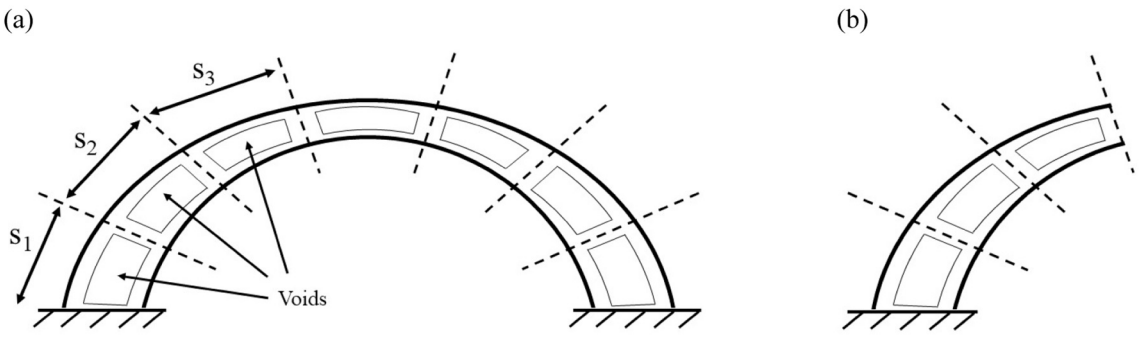

Fig. 3. Modular arch design at (a) fully assembled stage and (b) partially assembled stage.

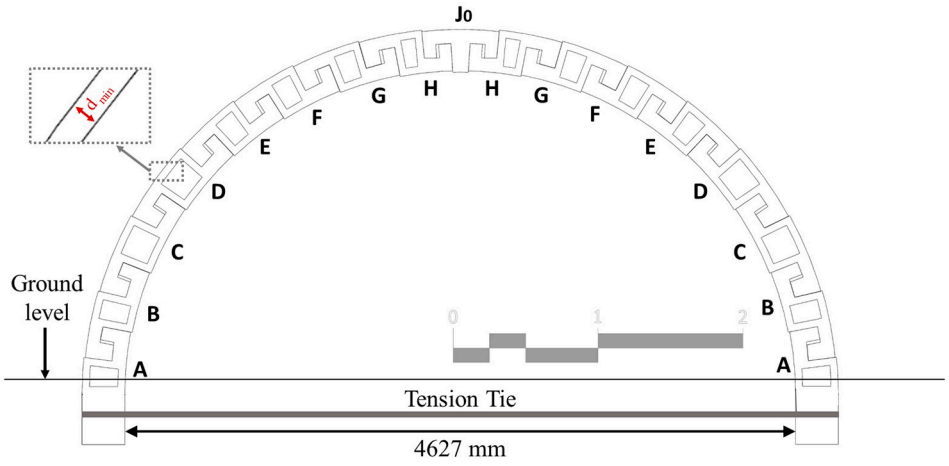

Fig. 4. Dimensions of Arch 1 (scale bar in meters).

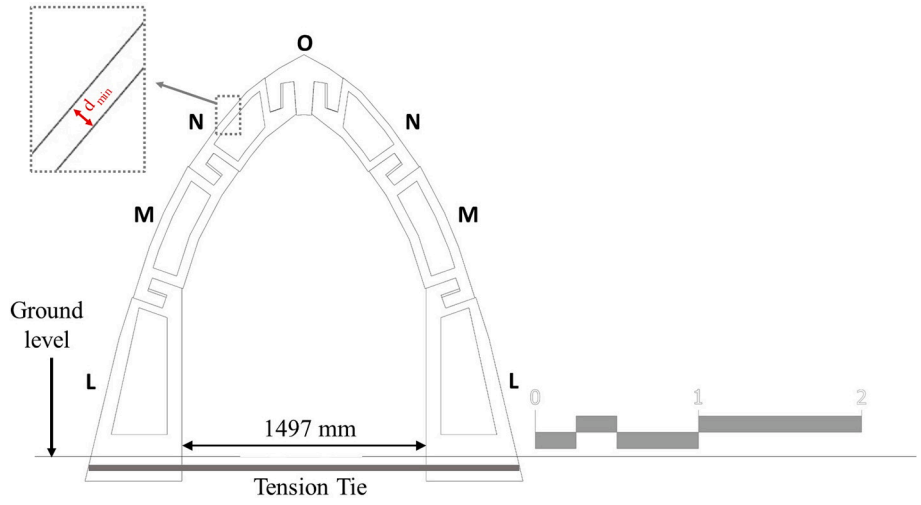

Fig. 5. Dimensions of Arch 2 (scale bar in meters).

which could be made by stacking 3D-printed concrete layers without a need to print overhanging concrete. Different from typical modular arches having relatively slender and curved shapes [13], the proposed arch was segmented into relatively prismatic modules, which could more efficiently occupy space for storage or during transportation [18].

To achieve a robust segment-to-segment assembling process for the arch, the geometries at the segment boundaries to be connected by adjacent segments were customized as hook-shaped geometry that provided an interlocking mechanism between adjacent element (Figs. 4 and 5). A nominal 10 mm (Arch 1) or 7 mm (Arch 2) clearance was allowed between the interlocking features of the segments. Examples of a well aligned and slightly misaligned segment-to-segment interlock are shown in Fig. 6a and b respectively, with both having a clearance between adjacent blocks. The hook shape interlock guided the segment-to-segment connection and the clearance allowed a reasonable amount of variability of the extruded bead width to be accommodated (Fig. 6a). Using relatively small size of clearance could effectively limit misalignment of segments, because the relative rotation between

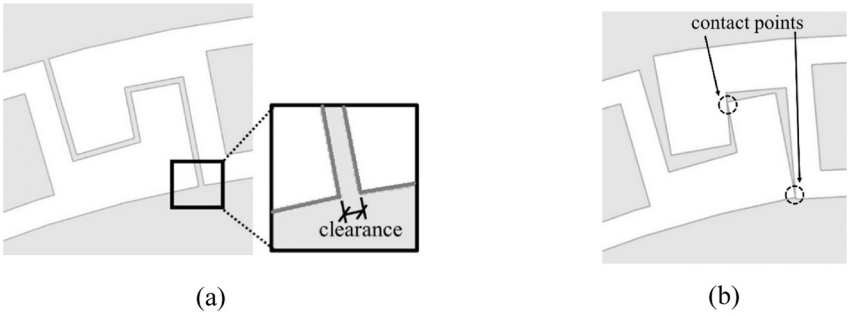

Fig. 6. (a) Clearance between blocks illustrated with the example of blocks G and H in Arch 1; (b) interlocking mechanism limiting relative rotation between adjacent blocks.

adjacent segment could increase until the clearance was closed at two contact points between adjacent segment (as shown by Fig. 6b). During assembling of adjacent blocks, epoxy mortar was to be applied in such clearance to provide proper segment-to-segment bonding; this was needed because the size of the nozzle used in this study did not permit fine-grained printing required to produce the sharp edges for exact fit between adjacent blocks.

The equilibrium equations in thrust-line analysis only hold under the situation where the structure or ground below the arch can provide horizontal reaction against the horizontal component force of the inclined compressive force acting along the thrust-line [21]. In the cases of insufficient reaction in horizontal direction, installing a metal-based, horizontal tension tie at the bottom of the arch structure is a common solution to providing additional reaction ensuring that the arch above is compression-dominated [37]. Since the design approach in this paper is for incorporating the arches on top of wide variety of grounds that are either capable or not capable to provide enough amount of horizontal reaction supporting the arches, there is a need to consider the following two scenarios for the proposed arch structures with different ground conditions:

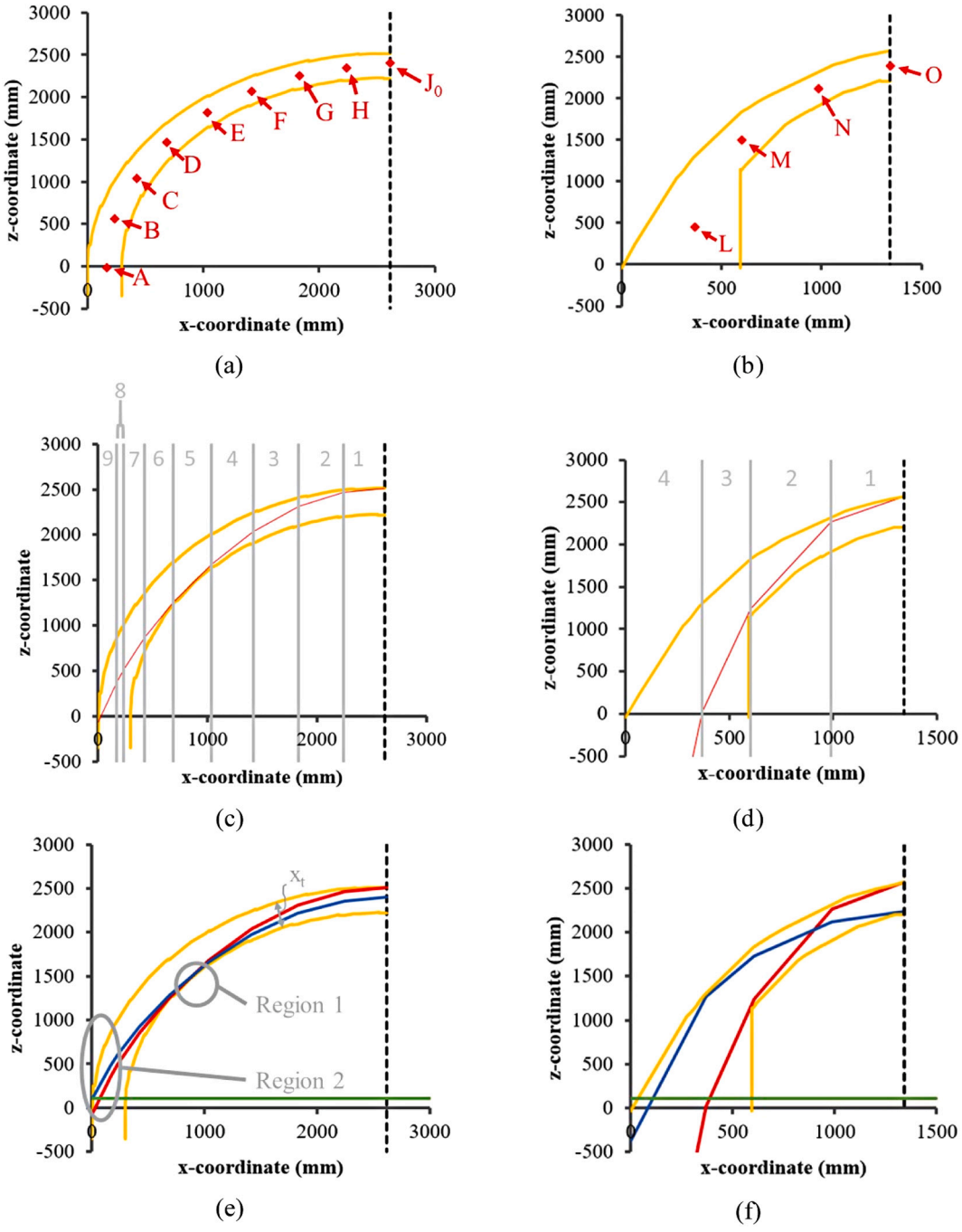

Fig. 7. Thrust-line analysis. Centers of gravity of (a) Arch 1 and (b) Arch 2; thrust-lines for minimum admissible horizontal thrust *H* for (c) Arch 1 and (d) Arch 2; thrust-lines for both minimum (red) and maximum (blue) admissible *H* for (e) Arch 1 and (f) Arch 2. (Yellow lines show the boundaries of the structure; black dashed lines show the axes of symmetry of the structures; green lines in (e) and (f) show the ground; red lines show the thrust-line for minimum admissible *H*; blue lines show thrust for maximum admissible *H*.) (For interpretation of the references to colour in this figure legend, the reader is referred to the web version of this article.)

(I) The ground is strong enough to provide the horizontal reaction fully without the need for tension tie. In this case, there is no need to install the tension tie so the tension tie below the proposed arches can be removed.
(II) The ground is not strong enough to provide the horizontal reaction fully so the tension tie needs to be installed to provide full or partial horizontal reaction.

To include the considerations from (II), the proposed design needs to provide a flexibility to allow incorporation of a tension tie below ground level at the base of Arch 1 (Fig. 4) and 2 (Fig. 5) in case additional reaction force is needed. The total magnitude of the horizontal reaction needed is determined by the geometry of the arch superstructure in thrust-line and strength analysis. Because the ground in (I) and the ground-tension tie assembly in (II) both provide the full amount of horizontal reaction, the arch to ground anchorage points in both (I) and (II) act as fixed supports. Since such fixed supports are applied as a boundary condition in both thrust-line and strength analyses in this paper, the analysis results are applicable to both scenarios (I) and (II). Arches 1 and 2 developed based on the iteration design/analysis process between (i), (ii) and (iii) will be used for demonstrating the detailed process for thrust-line and strength analysis respectively in Sections 2.1.1 and 2.1.2.

2.1.1. Thrust-line stability analysis and arched shape selection

Thrust-line analysis was incorporated into the design and analysis iteration process to obtain the arched layouts of Arches 1 (Fig. 4) and 2 (Fig. 5). In such analysis, a typical concrete density of 2250 kg/m^3 [1,38,39] was used. The weight of the epoxy mortar within the segment-to-segment clearance was negligible and hence it was ignored in the analysis. Due to symmetry of the arch, only one side of each arch needed to be analyzed to confirm that the arch was compression-dominated. Only the self-weight of the blocks was considered and the range of horizontal thrust forces, H (either provided by the tension tie, the ground or both) letting the structures remain stable, was established. The size of the range of admissible H was taken as a proxy for the robustness of the structure to perturbations during manufacturing or assembly [21]. Details of the analysis procedure are given in Section S2 of the Supplementary Information (Appendix A) and the equations were set up in Microsoft Excel [40] to conducted the analysis. Results of the thrust-line analysis are illustrated in Fig. 7 and summarized in Table 1. In Table 1, maximum and minimum values for admissible H in Arch 1 and 2 are respectively normalized against the weights of key stones (W_{J_0} for Arch 1 and W_O for Arch 2) to provide a sense of relative magnitudes between H and key stone segment weights so H/W_{J_0} and H/W_O are reported. According to the shape of the arches, the centers of gravity of each blocks for Arch 1 and 2 are shown in Fig. 7a and b respectively. With the information (for example, on centers of gravity) and procedures in Section S2 of the Supplementary Information, the thrust-lines with minimum value of H could be calculated at different regions in Arch 1 and 2 as shown in Fig. 7c and d respectively. For Arch 1, the thrust-lines with maximum and minimum values of H are plotted together in Fig. 7e. The thrust-lines with maximum and minimum values of H for Arch 2 are plotted in Fig. 7f. Because a finite set of admissible thrust-lines was found for each arch and for each analysis case, the results confirmed that the arches were indeed compression-dominated and that they remained stable under their self-weight.

Based on various applications of arch with different design goals, different ways of geometry parameter adjustment and different design constrains could be incorporated into the iterative design-analysis process to provide the flexibility to produce very different arch designs. Under aesthetic considerations and cost constraints, ancient builders of historical architectures, such as Gothic, Roman and Islamic architectures, pioneered the building of 3-dimensional, spatial structures via intersecting slender overhanging arches with long spans and consistent depth, x_t (Fig. 2) [12,15,16,41,42]. Therefore, when deploying the approach in this paper, such characteristics for arch construction were taken as design constraint to develop the 2.5D arches to be used as components in 3D spatial structure. In the iterative design/analysis process, the depth (x_t) along arch span (shown in Fig. 7e) was first kept as a constant value of 295 mm, which was a width that could be achieved by 3D-printing 12 pieces of parallel concrete filaments (26 mm of individual filament width and 13.1% of width for overlapping at the interfaces between adjacent filaments). With 295 mm of arch depth, the shape adjustment was started from an arch with a span-to-H$_r$ (H$_r$ is rise of arch as shown in Fig. 2a) ratio of 2.7, which was a typical ratio for arch with relatively large span [43]. However, this relatively shallow arch was not qualified as a compression-dominated structure based on thrust-line analysis, because its shape was too flat to allow a completed compression load transfer pathway from arch top towards the foundation. Therefore, the shape adjustment was further conducted by reducing the span-to-H$_r$ ratio until it reached 2.07 used for the final design of Arch 1, which passed the check from thrust-line analysis as discussed previously.

The high slenderness of Arch 1 led to a relatively small range of admissible thrust-lines (Fig. 7e). The relatively large span of this arch led to shallow slops of its thrust-lines (Fig. 7e), accompanied by larger magnitude of horizontal thrust (H reported as normalized form in Table 1), which was the horizontal component force for the compressive force along the thrust-lines. In this case, the horizontal thrust induced by Arch 1 needed to be resisted by the ground or structure below it and could be reduced by adjusting the arch geometry [21,37]. However, such adjustment might contradict some of the design goals and constraints. For example, to get a steeper thrust-line with reduced magnitude of horizontal thrust, one could gradually adjust the Arch 1 boundaries, the extrados and soffit lines, to gradually approach the geometry of Arch 2, an example of pointed arch, which typically induced a steeper thrust line [21]. In this case, Arch 2 design did reduce the magnitude of horizontal thrusts (H reported as normalized form in Table 1) and, due to its tapered foundation blocks, provided a wider range of admissible thrust-lines (Fig. 7f). With such a characteristic, Arch 2 was more likely to remain compression-dominated and stable even if the compressive load path varied due to possible dimensional errors or misalignment of blocks. However, the lower span, lower slenderness and inconstant depth (x_t) of Arch 2 contradicted the design goals and constraints. On the other hand, Arch 1 was compression dominated based on thrust-line analysis and satisfied all design criteria. Therefore, Arch 1 was selected as the 2.5D arch to be further analyzed for developing the 3D intersecting arch structure.

When there was a need to improve the stability of Arch 1-like designs under compression, the proposed approach provided the flexibility to make minor geometry adjustment. If the constraint of fixing arch depth along the span was slightly alleviated, x_t could be adjusted by moving the arch boundary at Region 1 (Fig. 7e) in the negative z and positive x directions to allow several steeper minimum thrust-lines to be admissible, or by moving the arch boundary at Region 2 (Fig. 7e) in the negative x direction to allow maximum-thrust-lines with more gentle slopes to become admissible [21]. Gradually adjusting the arch shape from Arch 1 (2.07 of span-to-H$_r$ ratio) to Arch 2 (0.90 of span-to-H$_r$ ratio) would sequentially generate many intermediate arch shapes with gradual decrement of span-to-H$_r$ ratio. An example of such intermediate case is shown by Fig. 8. One of the design constraints was that the total width of 2 concrete filaments extruded side-by-side was to be used as the minimum dimension (shown as d_{min} in Figs. 4 and 5) for the arch. Therefore,

Table 1
Summary of thrust-line analysis results.

Arch 1		Arch 2	
Minimum H/W_{J_0}	Maximum H/W_{J_0}	Minimum H/W_O	Maximum H/W_O
4.01	4.51	0.59	1.54

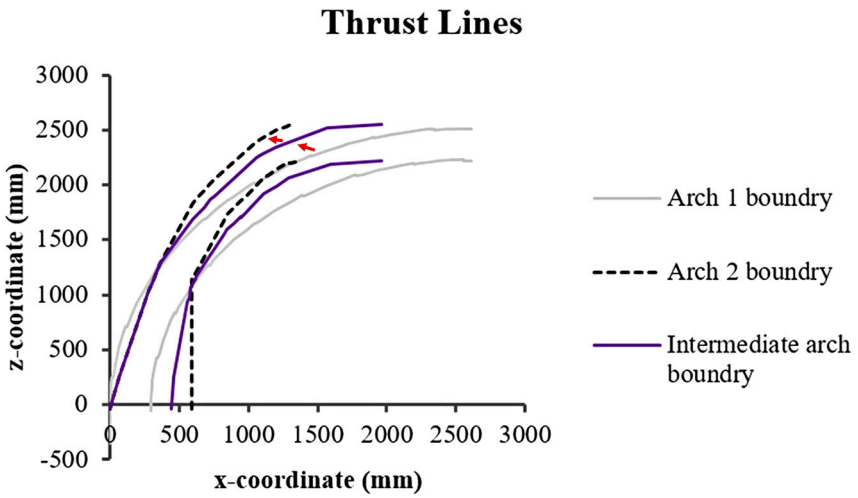

Fig. 8. An Intermediate case for shape adjustment between Arch 1 and 2.

Arch 1, Arch 2 and the intermediate arch geometries between them had a fixed value of minimum dimension within the arch. Changing the shape of the arch in this way would increase the range of admissible thrust-lines due to reduction of span-to-H_r ratio. As a result, the intermediate arch geometries and Arch 2 were qualified as compression-dominated structures based on thrust-line analysis. This shape adjustment scheme could further improve the stability of the arch but it allowed the arch thickness x_t to change along the arch span. If a specific curvature profile was required in an arch and its thickness x_t was strictly constrained, it might be possible to optimize the masses of individual segments in the arch to direct the thrust-line within the structure [23]. Such an approach would be enabled by the geometric freedom of concrete 3D printing and its ability to vary the sizes of internal voids in the fabricated blocks.

2.1.2. Assembling process and strength analysis at partially and fully assembled stages

In the proposed approach, the arch assembling process started with separately assembling left and right sides of the arch (segments A to H in Fig. 4 or segments L to N in Fig. 5) on the ground with adjacent segments glued together via epoxy mortar (as demonstrated via the lab prototyping presented in Section 3.1). After the shapes of left and right half arches were fixed by the epoxy mortar, they were erected and connected with each other via inserting the key stone (segment J_0 in Fig. 4 or segment O in Fig. 5) between them.

Until the two sides of the erected arch met and the keystone was in place, the structures were not compression-dominated; instead, blocks experienced bending moments exerted by their own weights and that of any blocks above them. These moments translated to local tensile and compressive stress fields within the blocks. Because the tensile strength of concrete was typically ~10 times lower than its compressive strength, an analysis must be conducted to check whether tensile fracture was possible during construction.

Typical values [1,38,39,44,45] of compressive strength (45 MPa), tensile strength (4 MPa), and density (2250 kg/m^3) for normal strength concrete were used in the strength analysis conducted by manual calculation. The weight of epoxy mortar within segment-to-segment clearance was negligible compared to the weight of concrete segments, and hence, was ignored in the calculation for strength analysis. For structural integrity of modular construction, it is important to identify the assembling stages with most critical load condition and find out the module and spot resisting highest stress at such stage. In Arch 1, the thinnest elements of each block had equal cross-sectional area, so it was apparent that the tensile stress in Element 1 in the foundation block was higher than other part of the partially assembled arch (Fig. 9). When

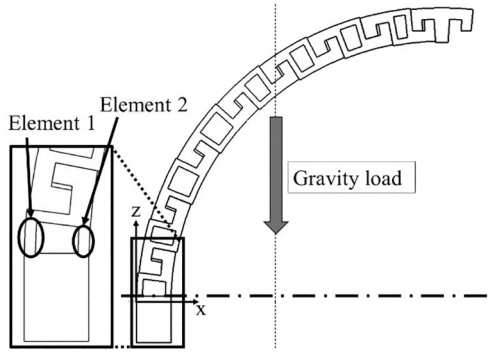

Fig. 9. Analysis for maximum bending loads and tensile stresses induced during the construction of Arch 1.

half of the arch was erected with keystone, but the keystone had not yet been connected to the other half of the arch (Fig. 9), the tensile stress in Element 1 reached a maximum value. Therefore, the strength analysis for partially assembled Arch 1 was to check if Element 1 fracture under such a maximum stress.

The total weight, W_p, of all the material above the bottom of Elements 1 and 2 (as indicated by dash-dotted line in Fig. 9) was assumed to act through $x = x_c$, the x-coordinate of the center of gravity of these blocks. Elements 1 and 2 had center positions $x = x_1$ and $x = x_2$ respectively, and the cross-sectional area of Element 1 was A_{cr}. Taking moments about the bottom of Element 2 ($x = x_2$), the tensile stress σ_1 in Element 1 satisfied:

$$W_p(x_c - x_2) = \sigma_1 A_{cr}(x_2 - x_1) \tag{1}$$

$$\Rightarrow \sigma_1 = \frac{W_p(x_c - x_2)}{A_{cr}(x_2 - x_1)} \tag{2}$$

For a half-assembled Arch 1, the values of x_c, W_p and σ_1 were respectively calculated as 1187 mm, 3050 N and 1.52 MPa based on the geometry of the concrete blocks, as was $A_{cr} = 7500$ mm^2. The maximum expected tensile stress σ_1 was far lower than the tensile strength of the material, 4 MPa, suggesting that the arch would not be expected to fracture during assembly.

As shown in Eq. (2), the distance between Element 1 and 2 is calculated as $(x_2 - x_1)$ and can significantly affect the maximum expected stress (σ_1) in Element 1. If one uses an alternative foundation block design with enlarged distance between Element 1 and 2, the maximum expected stress can be reduced. In general, 3D-printing allows

concrete blocks to be fabricated into hollow or cellular forms consist of truss-like concrete elements formed by extruded concrete filaments. For this partially assembled Arch 1 or other similar modular concrete structures with gravity center significantly offsets from the bottom support, foundation block is expected to experience relatively intense bending. By designing the foundation as a block consists of some vertical elements (similar to Elements 1 and 2 in Fig. 9) further from each other will help to provide a structural form that alleviates the maximum tensile stress induced by foundation block bending.

In addition to the strength analysis for partially assembled stage, the peak compressive stress experienced in the fully assembled Arch 1 was also estimated to confirm that it did not exceed the expected material strength. The first step was to compute the largest horizontal, H_{Max}, and vertical, L_V, thrust components acting through each foundation stone. H_{Max} was taken from the thrust-line analysis in Section 2.1.1, and L_V was the sum of the weights of all the blocks on one side of the arch and half the keystone weight, W_{key}. The resultant thrust, L_c, was computed as:

$$L_c = \sqrt{(H_{Max})^2 + (L_V)^2} \tag{3}$$

The peak compressive stress, σ_c, was then estimated by assuming L_c to act uniformly across A_b, the 7500 mm^2 of cross-sectional area of Element 1 of Arch 1 (Fig. 9).

$$\sigma_c = L_c / A_b \tag{4}$$

This assumption was conservative, because L_c would not in fact act normally to the cross-section of the element, and, moreover, some of the compressive load could also be carried by Element 2 of the foundation block of Arch 1. Therefore, σ_c would be an overestimate. As Table 2 shows, the expected compressive stresses were little more than 1% of the expected compressive strength, so compressive failure in Arch 1 was not anticipated. In addition to Arch 1, strength analysis could also be conducted for Arch 2 in a similar manner. However, since Arch 2 have been filtered out in the last section (Section 2.1.1), such arch design was not considered further in this study and its strength analysis procedure was excluded from this paper.

2.2. Development of 3D arch structure based on 2.5D arch element

The first step to use the 2.5D arch design of Arch 1 to develop the design of fully 3D structure was to adapt the keystone of Arch 1 to enable two pieces of Arch 1 to orthogonally intersect each other and form a 3D structure (Fig. 10). In the modified design, keystone J_0 was replaced by a new keystone, J (Fig. S2a in Supplementary Information in Appendix A), as well as a 'key cap', K (Fig. S2b in the Supplementary Information), that intersected with J to constrain the relative positions of the two arches. The double arch structure consisted of four pieces of half arches with same geometries as that for Arch 1. Similar to the assembling process for single Arch 1 structure mentioned in Section 2.1.2, the four pieces of half arch were separately assembled on ground first (Fig. 10a) and then, erected after the epoxy mortar applied between adjacent segments hardened and fixed the shapes of the arches (Fig. 10b). The erected half arches were set up two-by-two according to the order shown by Fig. 10c and d. Although the key stone and key cap both were 2.5D geometries fabricated from extrusion-based concrete 3D-printing, they were specially designed to perpendicularly interlock with each to form an arch crown structure with 3D geometry (Fig. 10f). Such a crossed crown structure could be inserted from top to link two pairs of half arches in two perpendicular directions. In this approach, individual arch components with 2.5D geometry could be assembled into a 3D structure of the double arch (Fig. 10e).

During the process of inserting and adjusting the key stone and key cap, the four pieces of erected half arch individually were under a case consistent to the critical case (Fig. 9) for strength analysis of partially assembled Arch 1 in the 2.5D case. On the other hand, the 3D structure consisted of two pieces of 2.5D structures of Arch 1 orthogonally intersecting each other after being fully assembled. Therefore, such 3D structure could be decomposed to the two pieces of Arch 1 for carrying out the 2D thrust-line analysis and 2D strength analysis to each piece of Arch 1 individually. This led to the same analyses as that conducted for fully assembled Arch 1 in the 2.5D case. Therefore, the double arch structure could be analyzed similarly as that for Arch 1. In this case, the results of thrust-line analysis (Section 2.1.1) and strength analysis (Section 2.1.2) carried out for the 2.5D structure of Arch 1 verified that the 3D structure of the double arch had no structural failure when it was partially assembled, and was a compression-dominated structure with good structural integrity after being fully assembled.

Table 2
Compression analysis of fully assembled Arch 1.

Arch type	W_{key} (N)	H_{Max} (N)	L_v (N)	L_c (N)	σ_c (MPa)
Arch 1	315.7	$4.51 \times W_{key} = 1423.8$	3285	3580.3	0.477

3. Feasibility study and lab prototyping of the 3D arch structure

To study the deployment feasibility of the double-arch proposed in this paper, a prototype of the double-arch with dimensions scaled down by a linear factor of 0.5 was fabricated and assembled. Comparing the dimensions of physical arch and its 3D-model provided dimensional offset information of individual arch segments from the 3D-printing fabrication and revealed how such dimensional offsets affect segment-to-segment assembling.

3.1. Material preparation, concrete 3D-printing and assembly of concrete blocks

Table 3 shows the concrete mix design for the mortar used in the arch prototype. The cement used was an ASTM (American Society for Testing and Materials) Type I 52.5 N (a standard cement meeting the strength class of 52.5 and having a normal early strength "N") [46]. In the mixture, silica sand with 0.1 of fineness modulus was used as a fine aggregate and ADVA 181 [47] (a high range, retarding, water-reducing admixture provided by GCP Applied Technologies Inc. [47]) was used as a superplasticizer (SP).

The equipment and process for concrete mixing and 3D-printing are shown in Fig. 11. The raw materials for concrete were first mixed by a pan type concrete mixer. Cement and sand were first added to the mixer for 2 min of dry mixing. Afterwards, water and superplasticizer were added to the mixture to let the mixer conduct another two sessions of wet mixing with 3 and 2 min of periods respectively. Before the second wet mixing session, the mixer was stopped and the concrete mixture attached to the internal wall and bottom of the mixer was manually scraped and scooped into the main batch of the mixture in the mixing container. This step was conducted before the next session of mixing to let the machine thoroughly mix the whole batch of material. After concrete mixing was completed, the concrete mixture was fed into a funnel of a concrete 3D-printing system, which consisted of a MAI®2-PUMP PICTOR-3D Concrete Printing Pump [48] attached to a 3-axis gantry system provided by Digital Construction Tech Kenyo [49]. Through the funnel, concrete flowed into the chamber of the concrete pump, which had a rotor stator system applying pressure to push concrete into and through the hose and eventually let concrete be extruded at the nozzle attached to the other end of the hose. Concurrently, the gantry system moved the nozzle (round opening with 20 mm of diameter) along the pre-assigned path under 45 mm/s of displacement rate to deposit the extruded concrete filament along the print path for 3D-printing each arch segment on the print bed as shown by Fig. 11. A total of 34 concrete blocks were 3D-printed. In each block, the layer thickness of 3D-printed concrete filament was designed as 12.5 mm and the actual layer thickness had an averaged value of 13.07 mm so the thickness of a concrete filament layer was deviated by 4.56%. As mentioned in Section

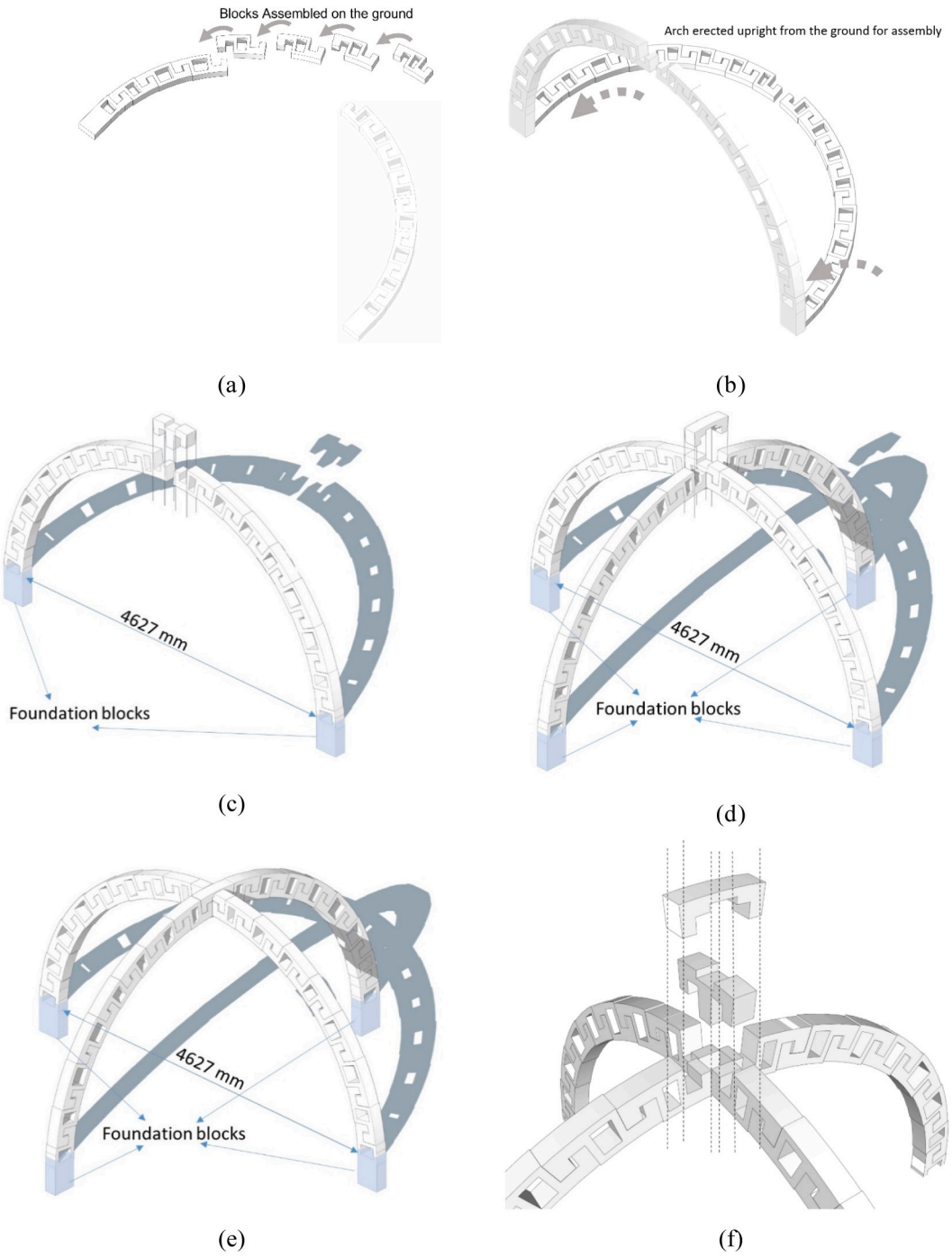

Fig. 10. Assembly of double arch. (a) Half arches are assembled on floor; (b) Half arches are erected (c) first arch is assembled and keystone J inserted; (d) second arch is assembled and key cap K is inserted; (e) complete intersecting arches; (f) exploded diagram of keystone J and key cap K.

Table 3
Mixture for mortar used for arch prototype.

Cement (g)	Sand (g)	Water (g)	Superplasticizer (mL)	Water-cement ratio
1000.0	603.1	400.2	2.00	0.400

Note that: Water-cement ratio $= \frac{\text{weight of water}}{\text{weight of cement}}$

2.1, the proposed arch design needed to provide a flexibility to install tension tie at the bottom of the arch structure. Therefore, during concrete 3D-printing, one metal pipe was allocated in each foundation concrete block to generate a hole in the block to allow later installation of tension ties. After 28 days of air dry curing, a typical curing condition for 3D-printed concrete [50,51], these modular blocks were assembled to form a double, intersecting arch structure as shown in Fig. 12.

Using 0.5 as a scale factor, the dimensions of the structure were changed by 0.5 times, which changed the volume and weight by 0.5^3 times and reduced the weight of half arch components from about 320 kg to 40 kg; this weight made it feasible for the printed components to be manually erected and assembled. The weight of 320 kg for a half arch in

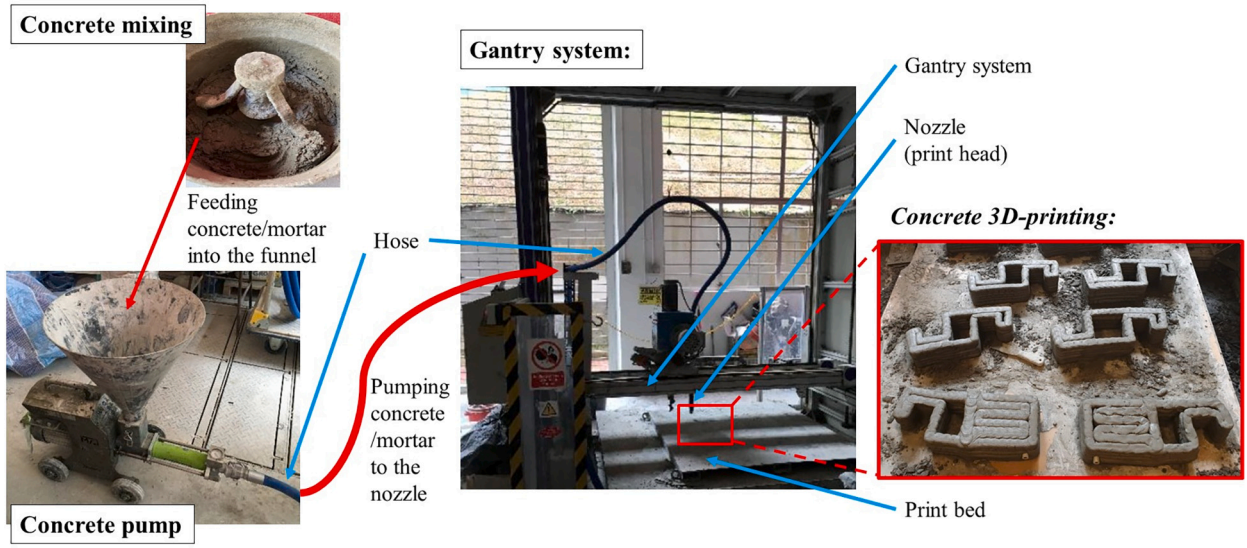

Fig. 11. Concrete mixing and 3D-printing.

full scale is still light enough for it to be erected by small construction lift or mini-crane [52]. Therefore, with basic equipment, the assembling process is at least scalable to the full scale of the structure proposed in this paper. The limit of this assembling process is determined by the scale of the arch structure. For assembling an ultra large scale arch structures with each piece of half arch having weight exceeding 800 kg, the typical mini-crane no longer has the capacity to lift the arch components [52].

Scaling down of dimensions for lab prototyping reduced the dimensions of the hook-shaped features by half, but this did not change the amount of dimensional error of the concrete filament extruded by specific concrete 3D-printer. Therefore, the scale factor of 0.5 would double the dimension error percentage in the hook-shaped interlock between adjacent segments, making the condition for arch assembling more stringent. In this case, the feasibility study was more conservative. Successful assembly in the lab under such a stringent condition was a good indicator of successful assembly of the full scale arch structure that would have about half of the dimensional error percentage in the hook-shaped interlock.

The assembling process in the lab prototyping followed the procedures in Fig. 10, where the two pairs of half arches were assembled on ground, followed by erecting half arches pair-by-pair and connecting the two pairs of half arches (Fig. 12e) via the assembly of key stone and key cap. When assembling the half arches on the floor (Fig. 12a), small amount of epoxy mortar, QUICSEAL 301, was applied between adjacent concrete blocks (Fig. 12f). To let the epoxy mortar harden, half arches was left on ground for 24 hours before erected. The first pair of half arches were erected first to form the first arch (Fig. 12b). Then, the third and four pieces of half arches were erected and connected to the first arch (Fig. 12c). Because the half arches were only erected after the epoxy mortar hardened and fixed adjacent concrete blocks together, the half arches had no sagging induced by relative movement between adjacent blocks after they were erected as overhanging components. During the assembling process, threaded rods were inserted through the holes in the foundation blocks to connect the foundation blocks at opposite ends of each arch together (Fig. 12d); these threaded rods acted as the tension ties. After fully assembling, this double arch resisting its self-weight became compression-dominated.

The purpose for the lab prototyping was to measure the dimensions from the physical prototype of the double arch and compare such dimensions with that from the 3D-model. Because the physical prototype had scale factor of 0.5, 3D-model with scale factor of 0.5 was used for such comparison, which is summarized in Table 4; this table is subdivided into three regions from top to bottom, and these regions respectively show: (1) dimension of the physical prototype, (2) dimension of the 3D model, and (3) dimensional offset between the physical prototype and the 3D model. As the blocks of the double arch are labeled according to Fig. S2 in the Supplementary Information (Appendix A), the first two columns in this table show the labels of adjacent blocks that interlocked together. As shown by Fig. 13, there was one lower block and one upper block at a segment-to-segment interface. Measurement was taken for the dimensions labeled from d1 to d12 in this figure and recorded in Table 4. For example, the 5th row in the table starts with blocks B and C respectively being indicated as lower and upper blocks for the typical interlock shown in Fig. 13, so this row records d1 to d12 at such interlock between blocks B and C. The dimensional offsets between these dimensions and that from the 3D-model (shown in the 2nd upper portion of the table) are calculated and shown in the bottom portion of the table. Positive and negative offsets respectively indicate larger and smaller dimensions in physical prototype compared to the dimensions in the 3D-model. Cumulative offsets are calculated as the sum of the offsets of certain dimension from the bottom to top interfaces. For example, the cumulative offset (−18.88) for d11 is calculated as the sum of the offsets for the d11 from the bottom to top interfaces.

In addition to measuring dimensions of physical blocks, the experimental works also included (1) measuring the clearances at segment-to-segment interlocks to find out the dimensional tolerance in individual segment 3D-printed and (2) measuring the overall horizontal dimension (side-to-side distance between foundation blocks at opposite sides) and vertical dimension (height to soffit of the arch) for the fully assembled prototype. For the 7 interfaces between the upper and lower blocks listed in Table 4, each interface had 5 clearances as shown in Fig. 13 so there were 35 clearances in total. 2 of such interfaces were fully covered by epoxy mortar after concrete block assembling and hence, were unmeasurable so the sizes of the remaining 33 clearances were measured. The averaged clearance and overall dimensions obtained from the measurements are compared with the dimensions for the proposed 3D CAD model in Table 5. The table shows not only the original CAD model designed using the proposed approach but also the CAD model with 0.5 of scale factor for comparison with the physical prototype. Comparing to the nominal clearance (5 mm) in the CAD model with 0.5 of scale factor, the averaged clearance (6.06 mm) measured from 33 segment-to-segment clearances in the lab prototype was 1.06 mm off, which was considered small compared to the overall horizontal dimension (2314 mm between opposite foundation blocks) and vertical dimension (1288 mm of height to soffit) of this CAD model. According to Table 4, the

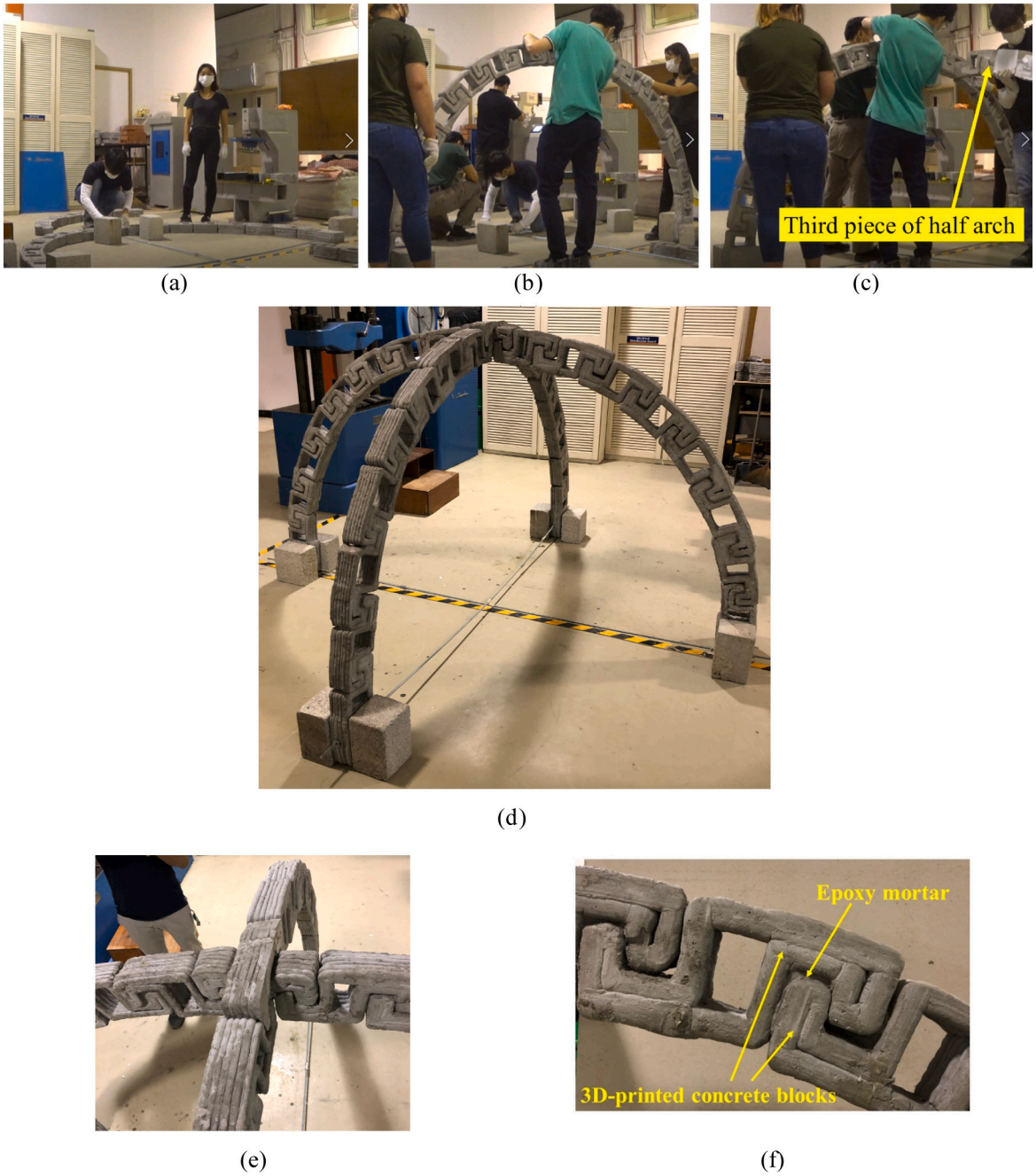

Fig. 12. (a) Assembled half arch on ground; (b) Erected arch; (c) Installation of half arch; (d) Assembled concrete double arch; (e) Intersection of the two arches; (f) Interlock between adjacent concrete blocks.

cumulative offsets for all dimensions were smaller than 56 mm and among the 12 cumulative offsets, only 5 of them exceeded 25 mm so the cumulative offsets were also very small compared to the overall arch dimensions. The relatively small values of cumulative offsets and differences of clearances in the lab prototype could still allow its overall dimensions to be very close to that of the CAD model.

3.2. *Insights for the prototype double-arch*

The physical prototype of two intersecting elliptical arches, shown in Fig. 12, was assembled successfully. The fully assembled structure demonstrated that one arch could support the other against out-of-plane motion. The overall dimensional tolerance of the concrete 3D-printing process provided an averaged inter-block clearances of 6.06 mm (with 2.27 mm of standard deviation (Table 5)) in this scaled-down prototype. This allowed the 3D-printed concrete blocks to be interlocked.

As shown by the schematic diagram in Fig. 14a, concrete filament was extruded by a round nozzle with an inner diameter (d_i) during concrete 3D-printing. Right after such filament being extruded from the nozzle opening, the filament was just shaped by the opening and hence, had a round cross section with a diameter same as d_i. After the filament was deposited on the print bed, the soft filament spread out in horizontal direction so the filament width increased from d_i to a larger concrete filament width (w_f). Based on the design of the arch components in the CAD model, the nozzle moving path was preassigned under an assumption that the concrete filament extruded along such a path had a designed filament width ($w_{f,d}$) as shown in Fig. 14b (a schematic diagram showing the top view for concrete filament extrusion). Therefore,

Table 4
Comparison of dimensions for proposed 3D structure design and physical model from lab prototyping.

Dimension measured from physical arch prototype													
Block		d1	d2	d3	d4	d5	d6	d7	d8	d9	d10	d11	d12	Thickness
Lower	Higher													
A	B	90.87	60.80	45.57	95.62	53.93	52.71	144.86	54.20	39.20	86.19	53.09	48.66	82.00
B	C	92.17	62.40	45.33	95.39	65.96	37.58	103.42	49.28	41.94	87.13	51.32	58.98	78.00
C	D	105.06	56.43	41.59	99.75	60.71	47.37	102.1	51.50	36.10	91.31	47.70	53.02	78.25
D	E	97.99	50.76	45.57	87.27	59.07	41.97	100.59	51.23	43.07	94.93	52.76	58.61	74.50
E	F	100.72	57.42	40.27	93.09	60.41	44.05	86.81	54.87	41.38	85.62	45.95	49.23	82.00
F	G	95.36	61.72	43.84	98.10	60.56	35.41	91.93	53.52	45.34	86.49	51.29	49.29	75.50
G	H	108.54	57.2	37.59	100.02	53.49	46.86	96.27	49.32	44.13	92.01	64.07	46.56	78.75

Dimension from 3D model (0.5 of scale factor)													
Block		d1	d2	d3	d4	d5	d6	d7	d8	d9	d10	d11	d12	Thickness
Lower	Higher													
A	B	97.01	50.11	47.28	97.58	65.17	45.00	102.58	45.00	47.72	92.49	55.00	54.88	75.00
B	C	96.98	50.21	47.24	97.58	64.67	44.97	102.58	45.00	47.67	92.50	55.03	47.67	75.00
C	D	97.27	50.54	49.93	97.50	65.12	45.00	102.50	45.00	50.07	92.78	55.00	55.12	75.00
D	E	97.50	50.00	46.82	97.14	64.79	45.48	102.58	45.00	47.70	92.50	55.01	55.21	75.00
E	F	97.49	50.08	47.28	97.58	64.88	45.00	102.58	45.00	47.72	92.97	55.00	54.89	75.00
F	G	97.01	50.00	47.25	97.58	65.24	44.99	102.58	45.00	47.70	92.50	55.01	54.77	75.00
G	H	97.01	50.00	47.20	97.58	65.24	44.99	102.58	45.00	47.64	92.50	55.01	55.21	75.00

Dimensional offset = (Dimensions of physical prototype) - (Dimension from 3D model)													
Block		d1	d2	d3	d4	d5	d6	d7	d8	d9	d10	d11	d12	Thickness
Lower	Higher													
A	B	−6.14	10.69	−1.71	−1.96	−11.24	7.71	42.28	9.20	−8.52	−6.30	−1.91	−6.22	7.00
B	C	−4.81	12.19	−1.91	−2.19	1.29	−7.39	0.84	4.28	−5.73	−5.37	−3.71	11.31	3.00
C	D	7.79	5.89	−8.34	2.25	−4.41	2.37	−0.40	6.50	−13.97	−1.47	−7.30	−2.10	3.25
D	E	0.49	0.76	−1.25	−9.87	−5.72	−3.51	−1.99	6.23	−4.63	2.43	−2.25	3.40	−0.50
E	F	3.23	7.34	−7.01	−4.49	−4.47	−0.95	−15.77	9.87	−6.34	−7.35	−9.05	−5.66	7.00
F	G	−1.65	11.72	−3.41	0.52	−4.68	−9.58	−10.65	8.52	−2.36	−6.01	−3.72	−5.48	0.50
G	H	11.53	7.20	−9.61	2.44	−11.75	1.87	−6.31	4.32	−3.51	−0.49	9.06	−8.65	3.75
Cumulative offset		10.44	55.79	−33.24	−13.30	−40.98	−9.48	8.00	48.92	−45.06	−24.56	−18.88	−13.40	–

when such a print path went along a boundary of a concrete block, the exterior gray line with $w_{f,d}/2$ of offset from the path overlapped with the boundary of the concrete block in the CAD model. However, when concrete 3D-printing was carried out physically, the rheological properties of concrete varied with time due to its ongoing cement hydration process. When the concrete mixture was more flowable right after extrusion, the concrete filament on the print bed spread out, leading to a larger filament width ($w_{f,2}$) which pushed the concrete block boundary outward and caused a positive dimension offset (i.e. dimension of lab prototype was larger than its CAD model). On the contrary, when concrete dried and became less flowable, concrete filament on the print bed spread out less, leading to a smaller filament width ($w_{f,1}$) and a negative offset (i.e. dimension of lab prototype was smaller than its CAD model). Therefore, the dimensional offsets in Table 4 consisted of both positive and negative values. As shown in Table 4, although some of dimensions, such as d7 and d8, were designed to be consistent across different segment-to-segment interfaces in the CAD model, such dimensions measured from the physical prototype fluctuated between different interfaces due to the positive and negative offsets induced by different rheological condition of the concrete mixture. According to [53], a dimensional offsets within ±15 mm was generally an acceptable offset for 3D-printed concrete components. Among the 91 values of dimensional offsets listed in Table 4, only two local offsets of 42.28 mm and −15.77 mm exceeded and marginally passed this range respectively. Considering the other 89 offsets were all within this range, the 3D-printing work of the arch structure met acceptable quality.

When the arch was assembled, the offsets for specific dimension accumulated from lower concrete blocks to top blocks so the cumulative offset had a pronounced effect on the overall dimension of the arch after assembling. Take dimension d6 as an example, positive offset of d6 in the lower blocks could cause the upper block to be further from the bottom block (as shown in Fig. 13) because a positive offset meant that this dimension in the physical block was larger than the design value. On the contrary, a negative offset of d6 resulted in the upper block and lower block being closer to each other. The offsets of d6 in the seven interlocks from bottom to top of the arch were respectively 7.71, −7.39, 2.37, −3.51, −0.95, −9.58 and 1.87 mm. In this case, the sum of all positive offsets was 11.95 mm and represented the cumulative effects of some lower blocks pushing upper blocks away. On the other hand, the sum of all negative offsets was −21.43 mm and represented the cumulative effects of other lower blocks allowing the upper blocks to be allocated closer to them. Herein, the effect from negative offsets with higher sum was more dominant but it was partially be compensated by the effect from the positive offsets. The cumulative offset (−9.48 mm) of d6 was calculated by adding the sums of positive (11.95 mm) and negative (−21.43 mm) offsets together, which showed how the effect of positive offsets compensated that from the negative ones. As a results, the cumulative offset (−9.48 mm) had smaller magnitude compared to the sums of both positive (11.95 mm) and negative (−21.43 mm) offsets. Having both positive and negative values of offsets was beneficial for limiting the magnitude of cumulative offset along the arch span. Therefore, this characteristic allowed the fully assembled arch to have overall dimensions very close to the design dimensions. Comparing the CAD file and lab prototype (both having scale factor of 0.5), the errors of overall dimensions, distance between opposite foundation blocks and height to soffit, were 1.56% and 0.15% respectively. As discussed in

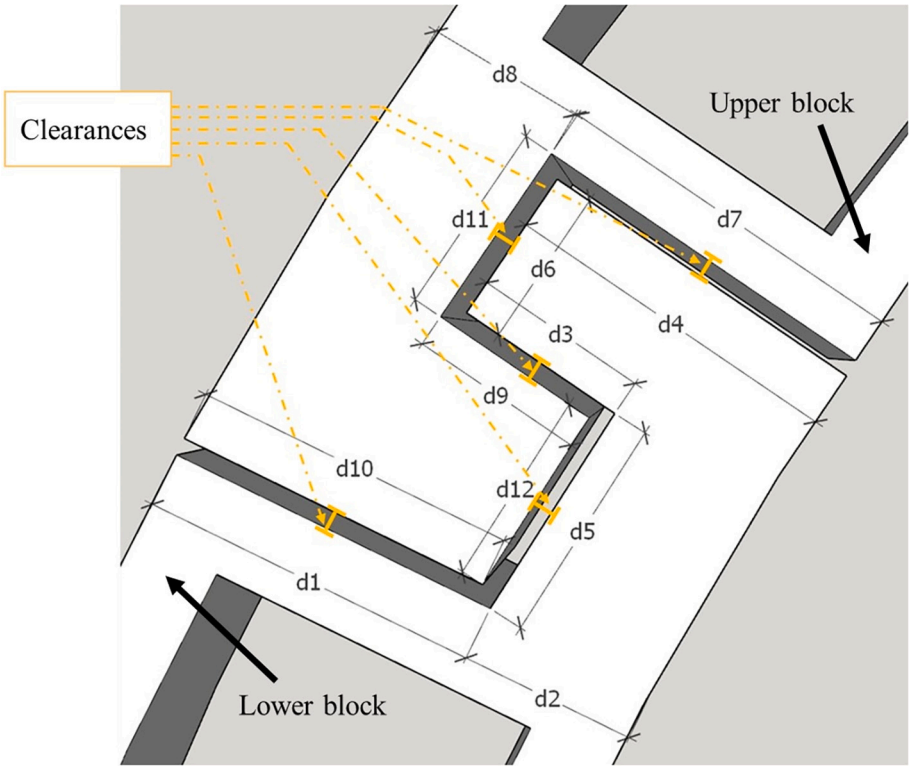

Fig. 13. Dimensions at segment-to-segment interface.

Table 5
Comparison of clearances and overall dimensions for proposed 3D structure design and physical model from lab prototyping.

Model	Scale factor	Clearance		Distance between Foundation blocks	Height to soffit
		Value	Standard deviation		
Proposed 3D CAD model	1	10 mm	–	4627 mm	2576 mm
	0.5	5 mm	–	2314 mm	1288 mm
Physical model from lab prototyping	0.5	6.06 mm (averaged value)	2.27 mm	2350 mm	1290 mm

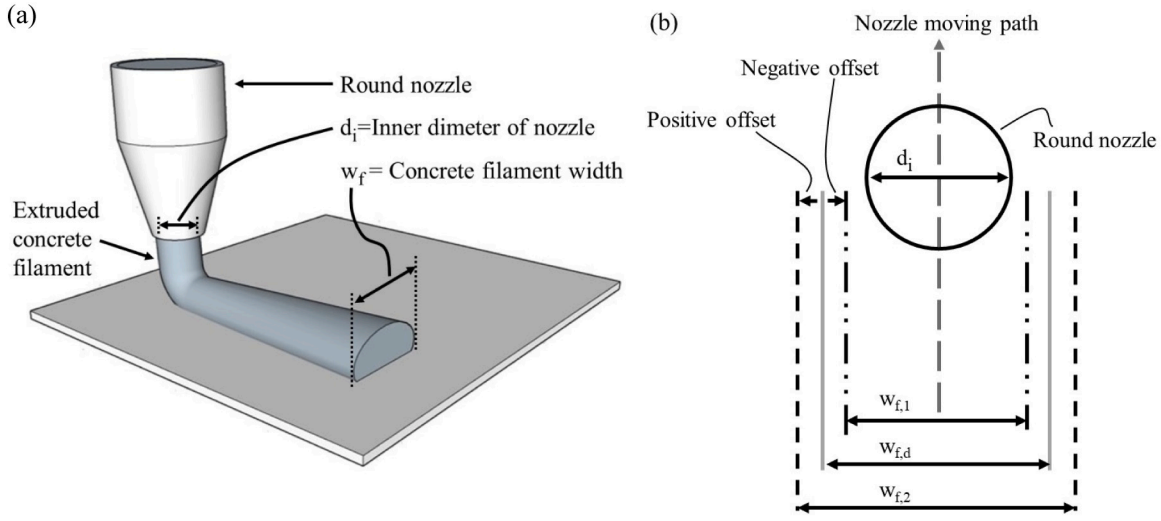

Fig. 14. Schematic diagram for concrete filament extrusion in (a) 3D view and (b) top view.

Section 3.1, the dimension offset from a specific type of concrete 3D-printer caused about double dimension error percentage at its hook-shaped interlock in the scale-down model (compared to that in the full scale structure). Successful assembly of the scale-down model indicated that such dimensional offset would cause even less pronounced difference between the designed and actual dimensions of the double-arch

structure in full scale. On the other hand, the thrust-line and strength analyses conducted in the design phase could ensure the structural integrity for such full scale structure with about 5 m in size, which was much larger than the print bed size of 1×1 m of the concrete 3D-printer. The dimension difference between the CAD and physical model could be addressed after the fabrication phase. According to the measurements from the physical prototype model, minor dimension adjustments were made to the arch segments in the CAD models, with and without the scale factor of 0.5.

Once the physical prototype of the double arch was completely assembled, one arch could support the other against out-of-plane overturning of the single arch and the epoxy mortar within inter-block clearance could effectively prevent sideways slippage locally occurred between adjacent concrete blocks. In situations where horizontal load (such as load induced by wind) could cause such inter-block slippage, the epoxy mortar with high strength (7-day compressive strength of 60 MPa and Tensile Strength of 13.8 MPa) could effectively resist the sideways movement between the modular blocks.

4. Conclusions

This paper introduced a new design approach with integration of fabrication and assembling of a compression-dominated, overhanging 3D structure formed by interlocking smaller, modular 2.5D concrete segments customized and fabricated by a concrete extrusion 3D-printer with 3-axis gantry robot and a flat print bed. Compared to concrete casting for complicated structure where customized formworks are needed, this approach of using formwork-free concrete 3D-printing with relatively low equipment requirement allows a rapid and simpler way of customizing the geometry of overhanging concrete structures based on the needs of different site and/or other structural design requirements.

In this paper, the feasibility of manufacturing and assembling in the proposed approach was successfully demonstrated by lab prototyping, where concrete segments were 3D-printed with vast majority of dimension offsets within an acceptable range of ±15 mm and assembled to form intersecting arches with overall dimensions very close to the designed dimensions. Such an arch structure had compression-dominated force transfer where tensile stress was minimized. Therefore, the design framework potentially alleviates the need to integrate steel reinforcement into some of the printed concrete structures. Because the individual blocks are in prismatic 2.5D geometries, the design framework is applicable to existing extrusion-based concrete 3D printing process where directly printing overhanging geometries is challenging. Moreover, the modular nature of the process allows for fabrication on print-beds with limited sizes, followed by easy transport to a construction site for assembly, which will involve erecting the partially assembled arch components.

Light construction equipment, such as small construction lift or mini-crane, can apply this assembling method for arch structures up to certain size limit where the weights of partially assembled arch components are within the lifting capacity of the machines. An important issue to be studied in the future is to develop a scheme to assemble the segment piece-by-piece in erected position to build the arch structure from bottom to the top, without application of any temporary falsework; in this case, the need for lifting and erecting partially assembled component can be avoided.

Thrust-line analysis confirmed that the arches proposed in this paper were compression-dominated. Strength analysis indicated that the concrete elements within these arches would not fracture during or after construction. In the future, the geometric versatility of concrete additive manufacturing can be exploited to create compression-dominated structures with more complex curvature profiles than those demonstrated here. An additional future challenge will be to extend the scheme to design fully three-dimensional, modular shell structures, such as domes. The aspiration to decompose 3D structures into interlocking elements that are individually prismatic and easily fabricated by printing will require further computational innovation. Nevertheless, the results of the present study indicate the feasibility of the design technique for arch-based structures, and augur well for the wider application of concrete 3D printing to the production of customized, compression-dominated structures.

Declaration of Competing Interest

The authors declare that they have no known competing financial interests or personal relationships that could have appeared to influence the work reported in this paper.

Acknowledgements

This work was supported by the National Research Foundation, Prime Minister's Office, Singapore under its IntraCREATE Seed Grant programme, grant NRF2016-ITS001-018, and its Singapore–Berkeley Building Efficiency and Sustainability in the Tropics (SinBerBEST) program. SinBerBEST is part of the Berkeley Education Alliance for Research in Singapore, which has been established by the University of California, Berkeley, as a centre for intellectual excellence in research and education in Singapore. The fund source had no involvement in study design, collection, analysis and interpretation of data; writing of this paper; and in the decision to submit the article for publication. Ms. Kai Qi Tang's help on assembling the 3D-printed prototype arch was appreciated. The authors declare no conflicts of interest.

Appendix A. Supplementary information

Supplementary information to this article can be found online at https://doi.org/10.1016/j.autcon.2022.104467.

References

[1] P.K. Mehta, P.J.M. Monteiro, Concrete: Microstructure, Properties, and Materials, McGraw-Hill, New York, NY, 2006. ISBN: 978-0-07-146800-8.
[2] D. Asprone, C. Menna, F.P. Bos, T.A. Salet, J. Mata-Falcón, W. Kaufmann, Rethinking reinforcement for digital fabrication with concrete, Cement and Concrete Research 112 (2018) 111–121, https://doi.org/10.1016/j.cemconres.2018.05.020.
[3] P. Kmiecik, M. Kamiński, Modelling of reinforced concrete structures and composite structures with concrete strength degradation taken into consideration, Archives of Civil and Mechanical Engineering 11 (2011) 623–636, https://doi.org/10.1016/S1644-9665(12)60105-8.
[4] B. Täljsten, A. Carolin, H. Nordin, Concrete structures strengthened with near surface mounted reinforcement of CFRP, Advances in Structural Engineering 6 (2003) 201–213, https://doi.org/10.1260/136943303322419223.
[5] M. Rossi, C.C. Barentin, T. Van Mele, P. Block, Experimental study on the behaviour of masonry pavilion vaults on spreading supports, Structures (2017) 110–120, https://doi.org/10.1016/j.istruc.2017.04.008.
[6] P. Block, J. Ochsendorf, Thrust network analysis: a new methodology for three-dimensional equilibrium, Journal of the International Association for Shell and Spatial Structures 48 (2007) 167–173. https://www.researchgate.net/profile/John-Ochsendorf/publication/237684255_Thrust_network_analysis_A_new_methodology_for_three-dimensional_equilibrium/links/581758fc08aeb720f6898f4a/Thrust-network-analysis-A-new-methodology-for-three-dimensional-equilibrium.pdf.
[7] V. Paris, A. Pizzigoni, S. Adriaenssens, Statics of self-balancing masonry domes constructed with a cross-herringbone spiraling pattern, Engineering Structures 215 (2020), 110440, https://doi.org/10.1016/j.engstruct.2020.110440.
[8] C.B. Costanzi, Z.Y. Ahmed, H.R. Schipper, F.P. Bos, U. Knaack, R.J.M. Wolfs, 3D printing concrete on temporary surfaces: the design and fabrication of a concrete shell structure, Automation in Construction 94 (2018) 395–404, https://doi.org/10.1016/j.autcon.2018.06.013.
[9] A. Liew, D.L. López, T. Van Mele, P. Block, Design, fabrication and testing of a prototype, thin-vaulted, unreinforced concrete floor, Engineering Structures 137 (2017) 323–335, https://doi.org/10.1016/j.engstruct.2017.01.075.
[10] M. Rippmann, A. Liew, T. Van Mele, P. Block, Design, fabrication and testing of discrete 3D sand-printed floor prototypes, Materials Today Communications 15 (2018) 254–259, https://doi.org/10.1016/j.mtcomm.2018.03.005.
[11] S. Huerta, Oval domes: history, geometry and mechanics, Nexus Network Journal 9 (2007) 211–248, https://doi.org/10.1007/s00004-007-0040-3.
[12] P. Carneau, R. Mesnil, N. Roussel, O. Baverel, Additive manufacturing of cantilever-from masonry to concrete 3D printing, Automation in Construction 116 (2020), 103184, https://doi.org/10.1016/j.autcon.2020.103184.
[13] T.V. Nguyen, J. Seo, J.-H. Ahn, A. Haldar, J. Huh, Finite element analysis-aided seismic behavior examination of modular underground arch bridge, Tunnelling

and Underground Space Technology 118 (2021), 104166, https://doi.org/10.1016/j.tust.2021.104166.
[14] M. Zoghi, D.N. Farhey, Performance assessment of a precast-concrete, buried, small arch bridge, Journal of Performance of Constructed Facilities 20 (2006) 244–252, https://doi.org/10.1061/(ASCE)0887-3828(2006)20:3(244).
[15] D. Theodossopoulos, B. Sinha, A.S. Usmani, Case study of the failure of a cross vault: Church of Holyrood Abbey, Journal of Architectural Engineering 9 (2003) 109–117, https://doi.org/10.1061/(ASCE)1076-0431(2003)9:3(109).
[16] C. Baggio, P. Trovalusci, 3D limit analysis of roman groin vaults, in: Proc. 16th International Brick and Block Masonry Conference (IBMAC 2016) Padova (Italy), 2016, pp. 1023–1028. https://iris.uniroma1.it/retrieve/handle/11573/1150178/1253880/Baggio_3D_2016.pdf.
[17] A. Borhani, N. Kalantar, Interlocking Shell. ACADIA (Association for Computer Aided Design in Architecture) 2020, 2020, pp. 226–231. Online, http://papers.cumincad.org/data/works/att/acadia20_226p.pdf.
[18] C.-H. Yang, S.-C. Kang, Collision avoidance method for robotic modular home prefabrication, Automation in Construction 130 (2021), 103853, https://doi.org/10.1016/j.autcon.2021.103853.
[19] J.P. Sousa, P.F. Martins, The robotic production of the GRC panels in the CorkCrete arch project-A stratified strategy for the fabrication of customized molds, in: 34th International Conference on Education and Research in Computer Aided Architectural Design in Europe (eCAADe), Oulu, Finland, 2016, pp. 153–160. http://papers.cumincad.org/data/works/att/ecaade2016_234.pdf.
[20] P. Mayencourt, C.T. Loraux, C. Robeller, E. Brühwiler, Y. Weinand, CNC-fabricated formwork for a UHPFRC thin folded plate arch. International Association for Bridge and Structural Engineering (IABSE) Conference, Geneva, Switzerland, 2015, pp. 1–8. https://os.zhdk.cloud.switch.ch/tind-tmp-epfl/6589df75-56f8-44a9-8c98-5fa43128e00a?response-content-disposition=attachment%3B%20filename%2A%3DUTF-8%27%27Full-Paper-IABSEGeneva15_PM_CL_final.pdf&response-content-type=application%2Fpdf&AWSAccessKeyId=ded3589a13b4450889b2f728d54861a6&Expires=1656749465&Signature=I1bMyST2amJXO8mcHFjFsb4NvvE%3D.
[21] D. Nikolic, Thrust line analysis and the minimum thickness of pointed masonry arches, Acta Mechanica 228 (2017) 2219, https://doi.org/10.1007/s00707-017-1823-6.
[22] N.A. Nodargi, P. Bisegna, Thrust line analysis revisited and applied to optimization of masonry arches, International Journal of Mechanical Sciences 179 (2020), 105690, https://doi.org/10.1016/j.ijmecsci.2020.105690.
[23] P. Block, M. DeJong, J. Ochsendorf, As hangs the flexible line: equilibrium of masonry arches, Nexus Network Journal 8 (2006) 13–24, https://doi.org/10.1007/s00004-006-0015-9.
[24] M. Rippmann, P. Block, Digital stereotomy: Voussoir geometry for freeform masonry-like vaults informed by structural and fabrication constraints, in: Proceedings of the IABSE-IASS Symposium, London, United Kingdom, 2011, pp. 1–8, https://doi.org/10.1080/10168664.2011.11985158.
[25] A.M. Bertetto, F. Riberi, Form-finding of pierced vaults and digital fabrication of scaled prototype, Curved and Layered Structures 8 (2021) 210–224, https://doi.org/10.1515/cls-2021-0020.
[26] F. Bos, Z. Ahmed, E. Jutinov, T. Salet, Experimental exploration of metal cable as reinforcement in 3D printed concrete, Materials 10 (2017) 1314, https://doi.org/10.3390/ma10111314.
[27] C. Gosselin, R. Duballet, P. Roux, N. Gaudillière, J. Dirrenberger, P. Morel, Large-scale 3D printing of ultra-high performance concrete–a new processing route for architects and builders, Materials & Design 100 (2016) 102–109, https://doi.org/10.1016/j.matdes.2016.03.097.
[28] Y.W.D. Tay, B. Panda, S.C. Paul, N.A. Noor Mohamed, M.J. Tan, K.F. Leong, 3D printing trends in building and construction industry: a review, Virtual and Physical Prototyping 12 (2017) 261–276, https://doi.org/10.1080/17452759.2017.1326724.
[29] G. De Schutter, K. Lesage, V. Mechtcherine, V.N. Nerella, G. Habert, I. Agusti-Juan, Vision of 3D printing with concrete—technical, economic and environmental potentials, Cement and Concrete Research 112 (2018) 25–36, https://doi.org/10.1016/j.cemconres.2018.06.001.
[30] L.Y. Shen, V.W.Y. Tam, C.M. Tam, S. Ho, Material wastage in construction activities–a Hong Kong survey. Proceedings of the First CIB-W107 International Conference—Creating a Sustainable Construction Industry in Developing Countries, 2000, pp. 125–131. https://www.researchgate.net/profile/C-Tam/publication/37812483_Material_wastage_in_construction_activities_-_a_Hong_Kong_survey/links/5604b1b808aea25fce31e79b/Material-wastage-in-construction-activities-a-Hong-Kong-survey.pdf.
[31] D. Lowke, E. Dini, A. Perrot, D. Weger, C. Gehlen, B. Dillenburger, Particle-bed 3D printing in concrete construction–possibilities and challenges, Cement and Concrete Research 112 (2018) 50–65, https://doi.org/10.1016/j.cemconres.2018.05.018.
[32] V. Mechtcherine, V.N. Nerella, F. Will, M. Näther, J. Otto, M. Krause, Large-scale digital concrete construction–CONPrint3D concept for on-site, monolithic 3D-printing, Automation in Construction 107 (2019), 102933, https://doi.org/10.1016/j.autcon.2019.102933.
[33] M.K. Mohan, A.V. Rahul, G. De Schutter, K. Van Tittelboom, Extrusion-based concrete 3D printing from a material perspective: a state-of-the-art review, Cement and Concrete Composites 115 (2021), 103855, https://doi.org/10.1016/j.cemconcomp.2020.103855.
[34] G. Ma, Z. Li, L. Wang, Printable properties of cementitious material containing copper tailings for extrusion based 3D printing, Construction and Building Materials 162 (2018) 613–627, https://doi.org/10.1016/j.conbuildmat.2017.12.051.
[35] B. Panda, S.C. Paul, N.A.N. Mohamed, Y.W.D. Tay, M.J. Tan, Measurement of tensile bond strength of 3D printed geopolymer mortar, Measurement 113 (2018) 108–116, https://doi.org/10.1016/j.measurement.2017.08.051.
[36] D. Asprone, F. Auricchio, C. Menna, V. Mercuri, 3D printing of reinforced concrete elements: technology and design approach, Construction and Building Materials 165 (2018) 218–231, https://doi.org/10.1016/j.conbuildmat.2018.01.018.
[37] E. Cescatti, F. Da Porto, C. Modena, C. Filippo, Ties in historical constructions: typical features and laboratory tests. 10th Structural Analysis of Historical Constructions, Leuven, 2016, pp. 1301–1307. https://www.researchgate.net/publication/308209956.
[38] S. Iffat, Relation between density and compressive strength of hardened concrete, Concrete Research Letters 6 (2015) 182–189. https://www.researchgate.net/profile/Shohana-Iffat/publication/289988475_Relation_Between_Density_and_Compressive_Strength_of_Hardened_Concrete/links/5693ec2b08ae820ff072967d/Relation-Between-Density-and-Compressive-Strength-of-Hardened-Concrete.pdf.
[39] H. Marzouk, Z.W. Chen, Fracture energy and tension properties of high-strength concrete, Journal of Materials in Civil Engineering 7 (1995) 108–116, https://doi.org/10.1061/%28ASCE%290899-1561%281995%297%3A2%28108%29.
[40] Microsoft Excel, Last acccess date: 2022-Feb-26; Available from: https://www.microsoft.com/en-us/microsoft-365/excel.
[41] A. Romano, J.A. Ochsendorf, The mechanics of gothic masonry arches, International Journal of Architectural Heritage 4 (2010) 59–82, https://doi.org/10.1080/15583050902914660.
[42] P. Fuentes, S. Huerta, Islamic domes of crossed-arches: Origin, geometry and structural behavior. Arch 10. 6th International Conference on Arch Bridges Fuzhou, 2010, pp. 11–13. https://oa.upm.es/4626/3/X-2276_PDF._Fuentes%2C_Huerta_2010._Islamic_domes_of_crossed-arches_Origin%2C_geometry_and_structural_behavior.pdf.
[43] L.S. Blinkov, E. Cosolo, S.N. Valiev, Rehabilitation of the Matsesta River Bridge, Russian Fed. Structural Engineering International 11 (2001) 181–183, https://doi.org/10.2749/101686601780346986.
[44] Standard Practice for Selecting Proportions for Normal, Heavyweight, and Mass Concrete, Last access date: 2022-July-1) indicated below: https://kashanu.ac.ir/Files/aci%20211_1_91.pdf.
[45] B. Chen, C. Li, L. Chen, Experimental study of mechanical properties of normal-strength concrete exposed to high temperatures at an early age, Fire Safety Journal 44 (2009) 997–1002, https://doi.org/10.1016/j.firesaf.2009.06.007.
[46] ASTM C150/C150M-19, Standard Specification for Portland Cement, Last acccess date: 2022-Feb-26; Available from: https://www.astm.org/c0150_c0150m-19.html.
[47] GCP Applied Technology, Last acccess date: 2022-Feb-26; Available from: https://gcpat.sg/en-gb.
[48] MAI®2PUMP PICTOR-3D, Last acccess date: 2022-Feb-26; Available from: https://www.mai.at/3d-printing/mair2pump-pictor-3d/.
[49] Digital Construction·Tech Kenyo, Last acccess date: 2022-Feb-26; Available from: https://m.ipfeibiao.com/trademark/view_42112560_19.html.
[50] J. Zhu, Z. Tao, F. Mansour, W. Chen, 3D printing cement based ink, and it's application within the construction industry. MATEC Web of Conferences, 2017, p. 02003.
[51] A. Lin, Y.K. Tan, C.-H. Wang, H.W. Kua, H. Taylor, Utilization of waste materials in a novel mortar–polymer laminar composite to be applied in construction 3D-printing, Composite Structures 253 (2020), 112764, https://doi.org/10.1016/j.compstruct.2020.112764.
[52] Sunaryo, A. Bahrun, L.O.M. Magribi, L. Hatani, Break even point concrete casting using hand-assembled mini-batching-plants and mini-crane in small islands and coastal areas, International Journal of Management and Education in Human Development 1 (2021) 74–82. https://ijmehd.com/index.php/OJSJournal/article/view/17/14.
[53] A. Anton, L. Reiter, T. Wangler, V. Frangez, R.J. Flatt, B. Dillenburger, A 3D concrete printing prefabrication platform for bespoke columns, Automation in Construction 122 (2021), 103467, https://doi.org/10.1016/j.autcon.2020.103467.